

Boosting CO₂ electrolysis performance by calcium oxide-looping combined with in situ exsolved Ni-Fe nanoparticles based on symmetrical solid oxide electrolysis cell

Received 00th January 20xx,
Accepted 00th January 20xx

DOI: 10.1039/x0xx00000x

www.rsc.org/

Yunfeng Tian,^{a, d} Yun Liu,^b Aaron Naden,^d Lichao Jia,^{a, c} Min Xu,^d Wen Cui,^d Bo Chi,^{a, c*} Jian Pu,^{a, c} John T.S. Irvine,^d Jian Li^{a, c}

Electrocatalysis CO₂ to valuable chemical production is one important strategy to combat global warming. Symmetrical solid oxide electrolysis cells have been extensively recognized for their electrolysis of CO₂ due to their high efficiency, low cost and reliability. Here, we propose a novel electrode with calcium oxide-looping and in situ exsolved Ni-Fe nanoparticles by a one-step reduction of La_{0.6}Ca_{0.4}Fe_{0.8}Ni_{0.2}O_{3-δ} (LCaFN). The CO₂ captured by CaO is electrolyzed in situ by Ni-Fe nanocatalysts. The cell with this special cathode shows higher current density (0.632 A/cm² vs 0.32 A/cm²), lower polarization resistance (0.399 Ω·cm² vs 0.662 Ω·cm²) compared with unreduced LCaFN cathode at the applied voltage of 1.3 V under 800 °C. The novel electrode offers a promising strategy for CO₂ electrolysis.

1. Introduction

Reduction of CO₂ emissions and conversion of CO₂ into high value-added chemical production are efficient strategies for limiting climate change. Today, numerous solutions are employed for CO₂ conversion such as chemical, photocatalytic and electrocatalytic methods.¹⁻⁵ Among them, solid oxide electrolysis cells (SOECs) have attracted significant interest due to their high efficiency and reliability.^{6, 7} In order to reduce manufacturing costs, the same material can be used both as the cathode and anode of SOECs, named as symmetrical solid oxide electrolysis cells (SSOECs) (Figure. S1). Further reduction of costs can be achieved by minimizing the preparation procedure and improving the compatibility of electrolyte/electrode interface.^{8, 9} However, the accompanying challenge is that the electrode of SSOECs must exhibit high electrocatalytic activity and good stability towards two simultaneous oxygen evolution reaction (OER) and CO₂ reduction reaction (CO₂RR), which puts higher requirements on the choice of electrodes. SSOECs electrode systems, including Sr₂Fe_{1.5}Mo_{0.5}O_{6-δ},^{10, 11} La_{0.3}Sr_{0.7}Fe_{0.7}Cr_{0.3}O_{3-δ},¹² La_{0.6}Sr_{0.4}Co_{0.2}Fe_{0.8}O_{3-δ},¹³ La_{0.3}Sr_{0.7}Fe_{0.7}Ti_{0.3}O_{3-δ}¹⁴ and MnCo₂O₄,¹⁵ have been explored.

However, low catalytic activity and poor stability at operation condition hinder their development although the glorious prospect of SSOECs.

The molecular shape of CO₂ is linear and its structure is considered as: O = C = O. A major challenge for enhancing the CO₂RR performance is to increase the capacity of CO₂ adsorption of SOEC cathode. Poor CO₂ adsorption capacity at the SOEC cathode will lead to starvation of CO₂ on the surface and therefore cause low electrochemical performance.¹⁶⁻¹⁸ Numerous studies have shown that introducing oxygen vacancies at the cathode surface could be an effective way to promote the chemical adsorption of CO₂.¹⁹⁻²¹ However, too strong adsorption of CO₂ on the cathode induced by oxygen vacancies hinders the electrocatalytic reactions in some cases. If the adsorption is strong, it is not favored for the activation of C=O bonds.²² Therefore, effective adsorption and activation of CO₂ is an important prerequisite for its direct electroreduction through SOEC.

Calcium oxide (CaO) is a conventional CO₂ adsorbent.^{23, 24} However, directly combining CaO or impregnating CaO into the electrode is not particularly beneficial for improving the electrochemical performance.^{25, 26} Fe-based perovskite oxides have stable structure, high conductivity, matching TEC with electrolyte.²⁷ Herein, we reported a novel perovskite oxide La_{0.6}Ca_{0.4}Fe_{0.8}Ni_{0.2}O_{3-δ} (LCaFN). When it is reduced in situ, CaO appears on the surface with a large number of Ni-Fe nanoparticles. On the one hand, CaO can be used as a reliable CO₂ adsorbent to improve the adsorption performance of the electrode. On the other hand, the in situ exsolved nano Fe-Ni alloys are beneficial to improving the electrocatalytic performance of the electrode. Therefore, the in situ exsolved Ni-Fe nanoparticles and CaO can form a synergistic effect that enhances the electrochemical performance of SSOECs.

^a Center for Fuel Cell Innovation, School of Materials Science and Engineering, Huazhong University of Science and Technology, Wuhan 430074, China.

*Corresponding author E-mail: chibo@hust.edu.cn

^b China-EU Institute for Clean and Renewable Energy, Huazhong University of Science and Technology, Wuhan 430074, China.

^c MOE Key Laboratory of Material Chemistry for Energy Conversion and Storage, Huazhong University of Science and Technology, Wuhan 430074, China.

^d School of Chemistry, University of St Andrews, St Andrews, Fife, KY16 9ST Scotland, UK.

† Electronic Supplementary Information (ESI) available: [details of any supplementary information available should be included here]. See DOI: 10.1039/x0xx00000x

2. Results and discussion

Refined XRD patterns of LCaFN and R-LCaFN powders (reduced in 5% H₂/N₂ at 800 °C for 5 h) are shown in Figure. 1(a) and Figure. 1(b), respectively. The diffraction peaks of LCaFN and R-LCaFN are almost identical, which indicates good stability of the LCaFN perovskite structure under reducing atmosphere. Moreover, there are some diffraction peaks at 26°, 44°, 52.3° and 74° corresponding to (100), (111), (200) and (220) lattice planes of FeNi₃ (PDF # 65-3244) as shown in Figure. 1(b). This reflects an abundance of Ni-Fe nanoparticles exsolved from the LCaFN backbone after reduction. In addition, there are peaks around 38° and 54°, indicating CaO in situ formed at the surface of R-LCaFN. This is because the solid solubility of Ca will decrease accompanying the exsolved FeNi₃ alloy. The unit cell of R-LCaFN is slightly larger than that of LCaFN (volumes of 58.91 Å³ and 58.02 Å³, respectively) because Fe³⁺ is transformed into Fe²⁺ with larger ionic radius (0.65 Å and 0.78 Å, respectively) under reducing conditions. The smaller R_p, wR_p and chi² indicate that the refinement results fit well with the patterns. There is a peak at 28° corresponding to CaCO₃ when R-LCaFN powders are calcined under CO₂ at 800 °C for 5 h. Interestingly, the CaCO₃ peak disappears and only CaO remains when these powders are treated in 5% H₂/N₂ for 0.5 h again since CaCO₃ has a lower decomposition temperature. To test the alternative thermal stability of the R-LCaFN powders, 7 cycles of heat treatment of R-LCaFN powders under CO₂ and 5% H₂/N₂ were measured, as shown in Figure. 1(c). The structure of R-LCaFN remains stable after 7 cycles, demonstrating that R-LCaFN operated in CO₂ atmosphere can be recovered by 5% H₂/N₂. Furthermore, R-LCaFN shows much larger specific surface area (5.341 m²/g) than LCaFN (4.353 m²/g) due to the abundant exsolved nanoparticles as shown in Figure. 1(d).

In terms of microstructure, the LCaFN powders present the smooth surface and uniform particle distribution as shown in Figure. 2(a) and (b) with compositions closely matching the

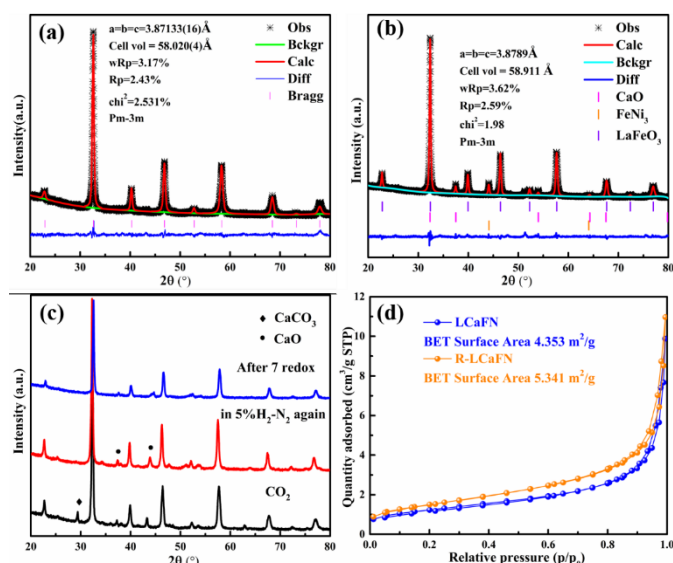


Figure. 1 Refined XRD patterns of LCaFN (a) and R-LCaFN (b), XRD patterns of R-LCaFN treated in CO₂ for 5 h, then treated in 5% H₂/N₂ for 0.5 h again and after 7 redox tests (c). BET curves of LCaFN and R-LCaFN (d).

expected stoichiometric ratio as measured by energy dispersive X-ray spectroscopy (EDS) (Figure. S2). A high-resolution scanning transmission electron microscopy (STEM) image of the LCaFN sample is presented in Figure. 2(c). The lattice fringe spacings of 0.216 nm and 0.153 nm can be indexed to (111) and (211) planes of the cubic perovskite LCaFN. The corresponding EDS mapping of the LCaFN sample illustrated in Figure. 2(d) confirms the homogeneous distribution of the composition elements. After reduction, densely packed nanoparticles are exsolved and embedded homogeneously into R-LCaFN as shown in Figure. 2(e)(f) and Figure. S3. High resolution STEM is used to identify its composition and the nanoparticle with lattice fringe space of 0.196 nm can be indexed to (111) plane of the FeNi₃ alloy as shown in Figure. 2(g). Besides, more aggregation of the element Ni and slight aggregation of Fe also proves the exsolved Ni-Fe nanoalloy as shown in Figure. 2(h) and Figure. S3-5. In addition, the enrichment of Ca element is labeled by the arrow, demonstrating the formation of CaO after reduction and it is further identified by EDS as shown in Figure. S6. These results are consistent with the previous analysis of XRD results.

EELS analyses are performed to reveal the electronic excitations from O 1s to O 2p bands in LCaFN and R-LCaFN as shown in Figure. 3(a). The feature of O K-edges is assigned to four main peaks: peak A results from hybridization of O 2p orbitals with Ni 3d and Fe 3d, while peak B corresponds to La 5d, Ca 3d, and peaks C and D are thought to contribute to Ni 4sp and Fe 4sp as well as scattering resonance of adjacent atoms.²⁷ It is noted that a lower intensity peak B forms together with the decreasing energy difference between peak A and peak B of R-LCaFN compared with LCaFN, indicating more oxygen vacancies formed after reduction.^{28, 29} Iodometric titration also confirms that the oxygen non-stoichiometry (δ) of the R-LCaFN (0.339) is larger than that of LCaFN (0.162). The fine structure of Fe L_{2,3}-edge is very effectual to determine the Fe oxidation state due to the transition from 2p_{3/2} and 2p_{1/2} electrons to unoccupied 3d orbitals; spectra from the two samples are shown in Figure. 3(b). The energy difference between the L₂ and L₃ peaks ($\Delta E_{L_2-L_3}$) and their intensity ratios (L₃/L₂ ratio) are related to the Fe oxidation state.³⁰ $\Delta E_{L_2-L_3}$ of LCaFN is 13.25 eV while 12.75 eV is measured for R-LCaFN and L₃/L₂ ratios of 6.03 and 5.95 are measured for LCaFN and R-LCaFN, respectively. The lower $\Delta E_{L_2-L_3}$ and L₃/L₂ ratio of the reduced sample both indicate a reduced valence of Fe and hence higher electron

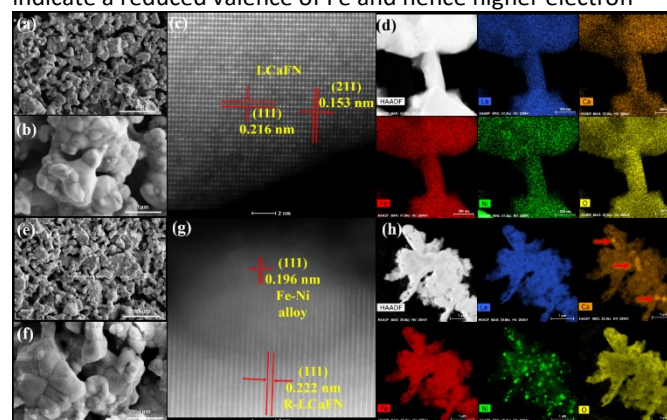


Figure. 2 SEM images (a) (b), high resolution STEM (c) and EDS-mapping (d) of LCaFN; SEM images (e) (f), high resolution STEM (g) and EDS-mapping (h) of R-LCaFN.

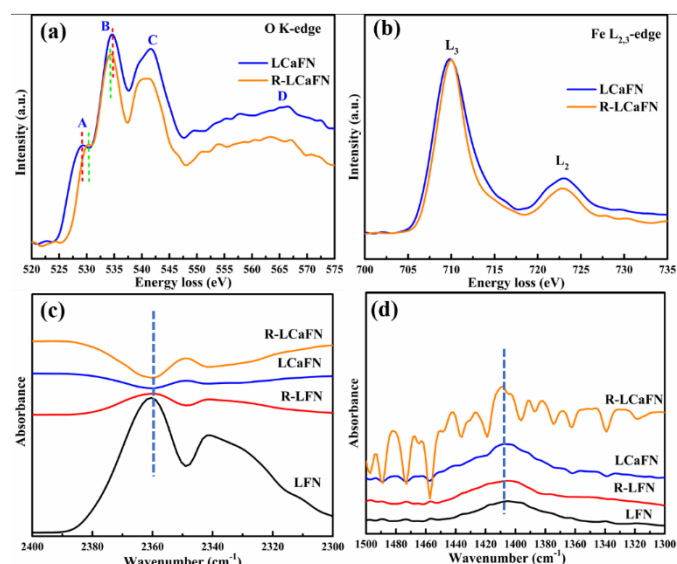


Figure 3 EELS profiles of LCaFN and R-LCaFN. (a) the O K-edges, (b) the Fe L_{2,3}-edges; in situ DRIFTS spectra of CO₂ adsorption (c) and reaction (d) of different samples.

density of Fe cations in the R-LCaFN.³⁰⁻³² This is an important observation since oxygen vacancies and electron density play significant roles in CO₂ electroreduction.³³

To investigate the adsorption performance of CaO and the catalytic effect of Fe-Ni alloy toward CO₂, in situ DRIFTS was used to characterize the CO₂ adsorption and reaction of LaFe_{0.8}Ni_{0.2}O₃ (LFN), R-LFN, LCaFN and R-LCaFN. Infrared scans for all the samples with CO₂ adsorption at room temperature display absorbance signals in two different infrared bands, shown in Figure. 3(c) and (d). Specifically, the infrared band of 2380-2300 cm⁻¹ is involved in CO₂ molecules on the sample surface, and 1450-1380 cm⁻¹ is typically associated with CO₃²⁻.^{34, 35} The peak upward represents CO₂ accumulation and the downward represents CO₂ consumption. It can be observed that the intensity of the CO₂ peak becomes weaker after Ca doping and reduction, demonstrating a strong interaction of CO₂ with the sample, forming carbonate which in turn causes the intensity of the CO₃²⁻ peak to increase gradually. These results indicate that R-LCaFN has significantly improved adsorption performance and catalytic activity compared to its as-prepared (not reduced) and LFN analogues.

I-V curves of two cells for pure CO₂ electrolysis at 800 °C are shown in Figure. 4(a). There exists a nonlinear relationship of the curve in the low voltage range, owing to the electrodes activation at the low current density.³⁶ It should be noted that the performance of R-LCaFN cell is considerably greater than that of the LCaFN cell, indicating the high catalytic activity of the R-LCaFN electrode. At 1.3 V, the LCaFN cell achieves current densities of 0.32 A/cm², whereas the R-LCaFN cell exhibits current densities of 0.632 A/cm², a remarkable 94% increase compared to the LCaFN cell. Crucially, this value is much higher than comparable systems with Pd single site-anchored La_{0.5}Sr_{0.5}FeO_{3-δ}-Ce_{0.8}Sm_{0.2}O_{2-δ} (0.58 A/cm²),³⁷ (Pr,Ba)₂Mn_{2-γ}Fe_γO_{5+δ} (0.32 A/cm²),¹⁶ La_{0.5}Sr_{0.5}Fe_{1-x}V_xO_{3-δ} (0.43 A/cm²)¹⁷ and Sr₂Fe_{1.5}Mo_{0.5}O_{6-δ} (0.6 A/cm²).³⁸

The electrochemical performance of R-LCaFN cell at different temperatures is shown in Figure. S7. EIS of two cells are test at

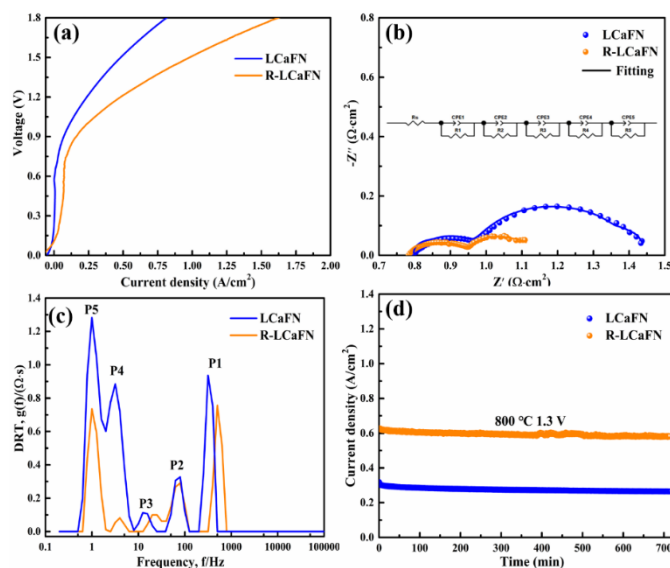


Figure 4 I-V curves of SSOECs with LCaFN and R-LCaFN electrode for CO₂ electrolysis at 800 °C (a), EIS (b), DRT plots (c) and stability test (d) of two cells at 1.3 V and 800 °C.

800 °C under 1.3 V as shown in Figure. 4(b). Two cells have similar ohmic resistance (R_s) because of the identical electrolytes and anodes. The cell with the R-LCaFN electrode shows a much lower polarization resistance (R_p) than that with the LCaFN electrode both in OCV and working condition (Figure. S8). The R_p value of the R-LCaFN cell is 0.399 Ω·cm² at 1.3 V, only 60.3% of that of the cell with the LCaFN cathode (0.662 Ω·cm²). Distribution of relaxation time (DRT) method is used to analyze the multiple electrode processes and the DRT results of the two cells are illustrated in Figure. 4(c). There are five peaks representing five electrochemical processes from high frequency to low frequency. That is, OER at the anode (P1), ion transport through the electrolyte (P2), the transfer of O²⁻ at cathode (P3), the CO₂ adsorption (P4) and electrochemical reduction (P5) processes.^{32, 39, 40} The area of five peaks represents the R_p of a specific process and the fitting results simulated by an equivalent circuit model (Figure. 4(b)) are summarized in Table S1. It is noteworthy that the lower peaks P4 and P5 demonstrate that both CO₂ adsorption and electrochemical reduction ability are enhanced via the in situ reduction process. CaO can effectively improve the adsorption performance of CO₂ and then the adsorbed CO₂ is efficiently electrolyzed by exsolved FeNi₃ nanoparticles. Attributed to the synergistic effect of nanoparticle and CaO in R-LCaFN cathode, the CO₂RR performance has a great improvement. The stability of the two cells is evaluated at 800 °C under 1.3 V as shown in Figure. 4(d). The R-LCaFN cell achieves a higher current density and stable performance during the entire 12 h run. Furthermore, the R-LCaFN cell still possesses the stable cell structure after test as shown in Figure. S9-10.

3. Conclusions

In summary, we propose a novel electrode with calcium oxide-looping and in situ exsolved Ni-Fe nanoparticles by one-step reduction of La_{0.6}Ca_{0.4}Fe_{0.8}Ni_{0.2}O_{3-δ} (LCaFN). The cell with this special cathode shows current density of 0.632 A/cm² under 1.3

V at 800 °C for CO₂ electrolysis, lower polarization resistance (0.399 Ω·cm²) and good stability. The synergistic effect of CaO and Ni-Fe nanocatalysts for the CO₂RR is clearly illustrated by the significant performance enhancement relative to as-prepared (not reduced with no nanocatalysts) and LFN analogues. This novel electrode therefore provides a promising strategy for CO₂ electrolysis.

Conflicts of interest

There are no conflicts to declare.

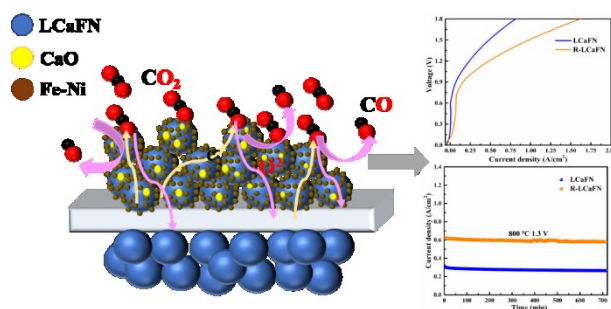
Acknowledgements

We gratefully thank for financial support from National Key Research & Development Project (2016YFE0126900), National Natural Science Foundation of China (51672095), Hubei Province (2018AAA057) and the EPSRC Capital for Great Technologies Grant EP/L017008/1. We are grateful to the China Scholarship Council for funding (201806160178). We also gratefully thank for Analytical and Testing Center of Huazhong University of Science and Technology which offers the SEM and XRD characterizations.

References

- J. Zhong, X. Yang, Z. Wu, B. Liang, Y. Huang, T. Zhang, *Chem. Soc. Rev.*, 2020, **49**, 1385-1413.
- Z. He, M. Cui, Q. Qian, J. Zhang, H. Liu, B. Han, *Proceedings of the National Academy of Sciences*, 2019, **116**, 12654-12659.
- C. Li, X. Tong, P. Yu, W. Du, J. Wu, H. Rao, Z.M. Wang, *J. Mater. Chem. A*, 2019, **7**, 16622-16642.
- X. Cui, P. Gao, S. Li, C. Yang, Z. Liu, H. Wang, L. Zhong, Y. Sun, *ACS Catal.*, 2019, **9**, 3866-3876.
- X. Zhang, X. Sun, S.-X. Guo, A.M. Bond, J. Zhang, *Energy Environ. Sci.*, 2019, **12**, 1334-1340.
- Y. Song, X. Zhang, K. Xie, G. Wang, X. Bao, *Adv. Mater.*, 2019, **31**, 1902033.
- T.L. Skafte, Z. Guan, M.L. Machala, C.B. Gopal, M. Monti, L. Martinez, E. Stamate, S. Sanna, J.A.G. Torres, E.J. Crumlin, *Nat. Energy*, 2019, **4**, 846-855.
- V. Kyriakou, D. Neagu, G. Zafeiropoulos, R.K. Sharma, C. Tang, K. Kousi, I.S. Metcalfe, M.C. van de Sanden, M.N. Tsampas, *ACS Catal.*, 2019, **10**, 1278-1288.
- Y. Tian, H. Zheng, L. Zhang, B. Chi, J. Pu, J. Li, *J. Electrochem. Soc.*, 2018, **165**, F17-F23.
- S. Hou, K. Xie, *Electrochim. Acta*, 2019, **301**, 63-68.
- Y. Wang, T. Liu, S. Fang, F. Chen, *J. Power Sources*, 2016, **305**, 240-248.
- B. Molero-Sánchez, P. Addo, A. Buyukaksoy, S. Paulson, V. Birss, *Faraday Discuss.*, 2015, **182**, 159-175.
- Z. Huang, H. Qi, Z. Zhao, L. Shang, B. Tu, M. Cheng, *J. Power Sources*, 2019, **434**, 226730.
- J. Xu, X. Zhou, J. Cheng, L. Pan, M. Wu, X. Dong, K. Sun, *Electrochim. Acta*, 2017, **257**, 64-72.
- L. Zhang, Y. Tian, Y. Liu, L. Jia, J. Yang, B. Chi, J. Pu, J. Li, *ChemElectroChem*, 2019, **6**, 1359-1364.
- J. Zhu, W. Zhang, Y. Li, W. Yue, G. Geng, B. Yu, *Appl. Catal. B*, 2020, **268**, 118389.
- Y. Zhou, Z. Zhou, Y. Song, X. Zhang, F. Guan, H. Lv, Q. Liu, S. Miao, G. Wang, X. Bao, *Nano Energy*, 2018, **50**, 43-51.
- W. Qi, Y. Gan, D. Yin, Z. Li, G. Wu, K. Xie, Y. Wu, *J. Mater. Chem. A*, 2014, **2**, 6904-6915.
- X. Zhang, Y. Song, F. Guan, Y. Zhou, H. Lv, G. Wang, X. Bao, *J. Catal.*, 2018, **359**, 8-16.
- L. Zhang, S. Hu, W. Li, Z. Cao, H. Liu, X. Zhu, W. Yang, *ACS Sustain. Chem. Eng.*, 2019, **7**, 9629-9636.
- Y. Li, Y. Li, Y. Wan, Y. Xie, J. Zhu, H. Pan, X. Zheng, C. Xia, *Adv. Energy Mater.*, 2019, **9**, 1803156.
- A.J. Medford, A. Vojvodic, J.S. Hummelshøj, J. Voss, F. Abild-Pedersen, F. Studt, T. Bligaard, A. Nilsson, J.K. Nørskov, *J. Catal.*, 2015, **328**, 36-42.
- S. Tian, F. Yan, Z. Zhang, J. Jiang, *Sci. Adv.*, 2019, **5**, eaav5077.
- A. Armutlulu, M.A. Naeem, H.J. Liu, S.M. Kim, A. Kierzkowska, A. Fedorov, C.R. Müller, *Adv. Mater.*, 2017, **29**, 1702896.
- M. Asamoto, S. Miyake, K. Sugihara, H. Yahiro, *Electrochem Commun*, 2009, **11**, 1508-1511.
- T. Takeguchi, Y. Kani, T. Yano, R. Kikuchi, K. Eguchi, K. Tsujimoto, Y. Uchida, A. Ueno, K. Omoshiki, M. Aizawa, *J. Power Sources*, 2002, **112**, 588-595.
- N. Ortiz - Vitoriano, I. R. de Larramendi, S. N. Cook, M. Burriel, A. Aguadero, J. A. Kilner, T. Rojo, *Adv. Funct. Mater.*, 2013, **23**, 5131-5139.
- B. Hua, M. Li, W. Pang, W. Tang, S. Zhao, Z. Jin, Y. Zeng, B.S. Amirkhiz, J.-L. Luo, *Chem*, 2018, **4**, 2902-2916.
- M. Li, B. Hua, J. Chen, Y. Zhong, J.-L. Luo, *Nano Energy*, 2019, **57**, 186-194.
- K.-H. Yang, J.-W. Kim, *Economic and Environmental Geology*, 2012, **45**, 189-194.
- Y. Yang, Y. Xiong, M.E. Holtz, X. Feng, R. Zeng, G. Chen, F.J. DiSalvo, D.A. Muller, H.D. Abruña, *Proceedings of the National Academy of Sciences*, 2019, **116**, 24425-24432.
- S. Hu, L. Zhang, H. Liu, Z. Cao, W. Yu, X. Zhu, W. Yang, *J. Power Sources*, 2019, 227268.
- Y. Jiang, Y. Yang, C. Xia, H.J. Bouwmeester, *J. Mater. Chem. A*, 2019, **7**, 22939-22949.
- L. Ye, M. Zhang, P. Huang, G. Guo, M. Hong, C. Li, J.T. Irvine, K. Xie, *Nat. Commun.*, 2017, **8**, 1-10.
- D. Dogu, K.E. Meyer, A. Fuller, S. Gunduz, D.J. Deka, N. Kramer, A.C. Co, U.S. Ozkan, *Appl. Catal. B*, 2018, **227**, 90-101.
- L. Yang, X. Xue, K. Xie, *Phys. Chem. Chem. Phys.*, 2015, **17**, 11705-11714.
- Y. Zhou, L. Lin, Y. Song, X. Zhang, H. Lv, Q. Liu, Z. Zhou, N. Ta, G. Wang, X. Bao, *Nano Energy*, 2020, **71**, 104598.
- C. Xu, S. Zhen, R. Ren, H. Chen, W. Song, Z. Wang, W. Sun, K. Sun, *ChemComm*, 2019, **55**, 8009-8012.
- H. Lv, L. Lin, X. Zhang, D. Gao, Y. Song, Y. Zhou, Q. Liu, G. Wang, X. Bao, *J. Mater. Chem. A*, 2019, **7**, 11967-11975.
- H. Lv, Y. Zhou, X. Zhang, Y. Song, Q. Liu, G. Wang, X. Bao, *J. Energy Chem.*, 2019, **35**, 71-78.

Table of contents



Boosting CO₂ electrolysis performance by calcium oxide-looping combined with in situ exsolved Ni-Fe nanoparticles based on symmetrical solid oxide electrolysis cell